Proceedings of the Project Review, Geo-Mathematical Imaging Group (Purdue University, West Lafayette IN),
Vol. 1 (2008) pp.165-182.

IMAGING AND ILLUMINATION WITH INTERNAL MULTIPLES

ALISON E. MALCOLM*, BJøRN URSIN†, AND MAARTEN V. DE HOOP‡

Abstract. If singly scattered seismic waves illuminate the entirety of a subsurface structure of interest, standard methods can be applied to image it. It is generally the case, however, that with a combination of restricted acquisition geometry and imperfect velocity models, it is not possible to illuminate all structures with only singly scattered waves. We present an approach to use multiply scattered waves to illuminate structures not sensed by singly scattered waves. It can be viewed as a refinement of past work in which a method to predict artifacts in imaging with multiply scattered waves was developed. We propose an algorithm and carry out numerical experiments, representative of imaging of the bottom and flanks of salt, demonstrating the effectiveness of our approach.

Key words. imaging, internal multiples, illumination, salt tectonics

1. Introduction. In this paper, we introduce a method of including multiply scattered waves in one-way wave equation based migration. The method has the potential to improve, in particular, images of the base of salt and of near-vertical structures such as salt flanks or faults. Our approach extends the work of [17] by including illumination in a series representation that models the data as a superposition of different phases. By explicitly including illumination in the series we identify those multiples which carry information about regions of the subsurface not illuminated by singly scattered waves.

Imaging with the one-way wave equation, based on multiply scattered waves, requires a "multi-pass" approach reminiscent of the generalized Bremmer series [10]. Turning waves can, in principle, also be accounted for in such an approach [30, 31]; see also Hale *et al.* [12]. In the multi-pass approach, starting at the surface (or top), waves are first propagated downwards and then stored at each depth; in the second "pass", starting at the bottom, reflection operators derived from the image are applied to the stored fields and the results are propagated, accumulatively, back upwards. To image steep reflectors, the (stored) downgoing wavefields are cross correlated in time with these upgoing fields, at each depth. Turning waves, however, can be incorporated in the one-way wave equation more naturally by introducing proper curvilinear coordinates (and associated Riemannian metric [26]).

The approach proposed in this paper integrates elements of Jin *et al.* [14], who developed a way to image near-vertical structures with doubly scattered waves, with Malcolm & De Hoop [17], who developed the inverse generalized Bremmer coupling series. Here, we modify this series to incorporate illumination effects to arrive at a method to generate partial images with different orders of multiply scattered waves. The final image is then assimilated from these partial images (cf. Figure 1). The inverse generalized Bremmer coupling series combines aspects of the Lippmann-Schwinger equation driven inverse scattering series developed by Weglein *et al.* [28, 27] with the generalization of the Bremmer series [5] developed by De Hoop [10]. Standard migration techniques typically take into account only the first term of these respective series, which is the single scattering assumption ubiquitous in seismic imaging. We confirm the reasoning behind our approach with numerical experiments. Our main interest, here, is imaging with "underside" reflections, but we generally consider internal multiples.

A method for imaging with surface-related multiples (primarily triply scattered waves) has been proposed by Berkhout & Verschuur [2]. They transform surface-related multiples into primaries with the "sources" at the surface reflection points. Elastic-wave surface reflections were also used by Bostock *et al.* [4] but then in the setting of teleseismic waves and passive sources. Doubly scattered waves have also been considered, for the purpose of imaging near-vertical structures. These have been referred to as "duplex", or "prismatic" waves, and were first discussed by Bell [1], directly followed by Hawkins [13], who discussed their influence on dip moveout (DMO) algorithms. Prismatic reflections have been exploited in a ray-theoretical framework, also in the context of travel time tomography, by several authors [1, 6, 18, 7, 8]. Bell [1] describes a method by which the location of a vertical reflector is optimized by reducing the travel

*Department of Earth Sciences, Utrecht University, Utrecht, the Netherlands.
†Department of Petroleum Engineering and Applied Geophysics, Norwegian University of Science and Technology, Trondheim, Norway.
‡Center for Computational and Applied Mathematics and Geo-Mathematical Imaging Group, Purdue University, West Lafayette IN, USA.

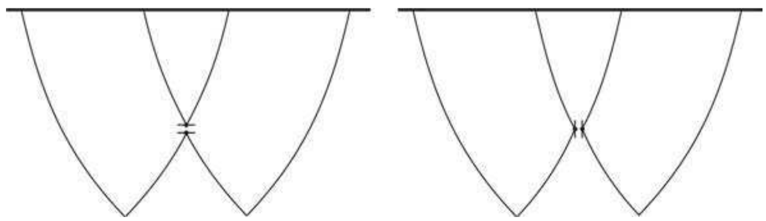

FIG. 1. *Assimilation of partial images. Examples of "topside" reflection (singly scattered waves, left), "underside" reflection (triply scattered waves, left) and "prismatic" reflections (doubly scattered waves, right) considered in this paper. The bottom reflector will be assumed to appear in the image of the first pass.*

time of the doubly scattered waves to an equivalent primary reflection. Marmalyevskyy [18] uses a Kirchoff method to carry out the imaging in which a near-horizontal reflector is picked and the reflection off this interface is included in the Green's function used in Kirchoff migration. A mathematical analysis of imaging with doubly scattered waves, related to the approach of Marmalyevskyy, has been carried out by Nolan *et al.* [20]. (Including certain reflectors in the velocity model in reverse-time migration to incorporate multiple scattering has been considered by Mittet [19].) In [6, 7, 8] the authors use the picked travel times of doubly scattered waves as part of a traveltime tomography procedure. The goal of their work is to provide an inversion framework that accounts for regions where the forward map for (modelling of) a particular event is "undefined". They choose the exploitation of doubly scattered waves as these waves are often recorded at only a subset of the receivers. In this case, primaries and doubly scattered waves are used in a joint inversion for both the velocity model and reflector locations; the doubly scattered waves are included by first identifying them as doubly scattered waves and then minimizing a travel time misfit between the computed (via raytracing) and true traveltimes.

Our approach requires neither the explicit identification of multiply scattered waves nor the manual location of near-horizontal reflectors. However, to avoid excessive computations, we introduce particular pseudodifferential cutoffs tied to the imaging conditions associated with doubly, triply, .. scattered waves, to implement our approach. These are reminiscent of the imaging condition used in reverse-time migration [3, 29], derived from directional wavefield decomposition.

The paper is organized as follows. We first review the basic structure of multiple scattering operators in the context of inverse scattering. We then introduce the notion of illumination decomposition. In Section 3 we discuss the formation of images with multiply scattered waves, making use of the illumination decomposition, and propose a corresponding algorithm. We carry out numerical experiments demonstrating the effectiveness of our approach in Section 4.

2. Multiple scattering: Image artifacts and illumination.

2.1. Directional decomposition. We consider acoustic wave propagation, governed by the system of equations

$$\partial_z \begin{pmatrix} u \\ \partial_z u \end{pmatrix} = \begin{pmatrix} 0 & 1 \\ -A & 0 \end{pmatrix} \begin{pmatrix} u \\ \partial_z u \end{pmatrix} + \begin{pmatrix} 0 \\ -f \end{pmatrix}, \tag{2.1}$$

where

$$A = A(z, x, \partial_x, \partial_t) = \partial_x^2 - c(z,x)^{-2}\partial_t^2, \tag{2.2}$$

u is the particle displacement, and f is the source density of injection rate; x denotes the "horizontal" coordinates, t is time, and z is the "depth" coordinate. The velocity c is assumed to be a smooth function. In n-dimensional seismics, $x = (x_1, \ldots, x_{n-1})$, $n = 2, 3$. To facilitate the decomposition of the wavefield into constituents that have been scattered a specific number of times, we split the wavefield into up- and down-going components, as in the development of the Bremmer series decomposition [10]. The analysis can be found in [25]. One introduces a z-family of decomposition operators, $\mathsf{Q}(z)$, with

$$U := \begin{pmatrix} u_+ \\ u_- \end{pmatrix} = \mathsf{Q}(z) \begin{pmatrix} u \\ \partial_z u \end{pmatrix}, \quad \begin{pmatrix} f_+ \\ f_- \end{pmatrix} = \mathsf{Q}(z) \begin{pmatrix} 0 \\ -f \end{pmatrix}, \tag{2.3}$$

that diagonalize system (2.1) according to

$$\mathsf{Q}(z) \begin{pmatrix} 0 & 1 \\ -A & 0 \end{pmatrix} \mathsf{Q}^{-1}(z) = \begin{pmatrix} \mathrm{i}B_+ & 0 \\ 0 & \mathrm{i}B_- \end{pmatrix}. \tag{2.4}$$

The operators $B_\pm$ are pseudodifferential operators (but not globally), and are often referred to as the single-square-root operators; for "true-amplitude" applications, their sub-principal symbols have to be taken into account. (For an introduction to the notion of wavefront sets and the calculus of pseudodifferential operators, see [24].) There are several different choices possible for the "normalization" of $\mathsf{Q}(z)$. We choose the vertical power flux normalization. Then the operators $B_\pm$ are self-adjoint, and the diagonal entries of the coupling operator, $\mathsf{Q}(z)\partial_z\mathsf{Q}(z)^{-1}$, are of lower order and can be neglected in leading-order "true-amplitude" applications. In this normalization, the decomposition operators attain the form

$$\mathsf{Q}(z) = \tfrac{1}{2} \begin{pmatrix} Q_+^*(z)^{-1} & -\mathcal{H}Q_+(z) \\ Q_-^*(z)^{-1} & \mathcal{H}Q_-(z) \end{pmatrix}, \tag{2.5}$$

where the $Q_\pm(z)$ are pseudodifferential operators, and $\mathcal{H}$ is the Hilbert transform in time. System (2.1) transforms, upon suppressing the down-up coupling, into a system of one-way wave equations,

$$\partial_z \begin{pmatrix} u_+ \\ u_- \end{pmatrix} = \begin{pmatrix} \mathrm{i}B_+ & 0 \\ 0 & \mathrm{i}B_- \end{pmatrix} \begin{pmatrix} u_+ \\ u_- \end{pmatrix} + \begin{pmatrix} f_+ \\ f_- \end{pmatrix}, \tag{2.6}$$

for the downgoing field, u_+, and the upgoing field, u_-. From (2.3) we find that $u(z,.) = Q_+^*(z)u_+(z,.) + Q_-^*(z)u_-(z,.)$, while $f_\pm(z,.) = \pm\frac{1}{2}\mathcal{H}Q_\pm(z)f(z,.)$. We introduce the Green's functions, $G_\pm$, for the one-way wave equations; we denote the corresponding solution operators, that is, one-way propagators, by the same symbols. Here, the evolution coordinate has become z. We then form the matrix

$$\mathsf{G} = \begin{pmatrix} G_+ & 0 \\ 0 & G_- \end{pmatrix}, \tag{2.7}$$

which is the down/up solution operator for the diagonal system (2.6).

To develop the scattering equations and formulate the inverse scattering problem, we decompose the velocity model into a background model $c_0(z,x)$, which is smooth and assumed to be known, and a contrast, $\delta c(z,x)$, which is to be determined. The contrast defines the perturbation,

$$\delta A = 2c_0^{-3}\delta c\, \partial_t^2 \tag{2.8}$$

of A in (2.2). With c_0 playing the role of c in the directional decomposition above, this naturally leads to the introduction of

$$V(z) = \mathsf{Q}(z) \begin{pmatrix} 0 & 0 \\ -\delta A(z,.) & 0 \end{pmatrix} \mathsf{Q}(z)^{-1}, \tag{2.9}$$

cf. (2.4). We then introduce $\widehat{V}$ according to $V = \widehat{V}\,\partial_t^2$. While neglecting the down-up coupling in the background model, the directional decomposition will facilitate the identification of different orders of multiply scattered waves. The total scattered field is written in the form

$$\begin{pmatrix} \delta u \\ \partial_z \delta u \end{pmatrix} = \mathsf{Q}(z)^{-1} \begin{pmatrix} \delta u_+ \\ \delta u_- \end{pmatrix}, \quad \delta U = \begin{pmatrix} \delta u_+ \\ \delta u_- \end{pmatrix}, \tag{2.10}$$

cf. (2.3). The equation for δU then reads [17, (41)],

$$(I - \partial_t^2 \mathsf{G}\widehat{V})\, \delta U = \partial_t^2 \mathsf{G}(\widehat{V}U), \tag{2.11}$$

which has the form of a Lippmann-Schwinger equation [16, 15], or

$$(I - \partial_t^2 \mathsf{G}\widehat{V})\,(U + \delta U) = U. \tag{2.12}$$

2.2. Recursions: Forward and inverse scattering. Starting from (2.11) we can now set up a recursion to generate multiple scattered waves:

$$\delta U_1 = \partial_t^2 \mathsf{G}(\widehat{V} U), \quad \delta U_m = \partial_t^2 \mathsf{G}(\widehat{V} \delta U_{m-1}),\ m = 2, \ldots, M \tag{2.13}$$

so that $\sum_{m=1}^{M} \delta U_m$ generates δU. (As compared with the generalized Bremmer coupling series, $\mathsf{G}(\widehat{V} \partial_t^2\ .)$ can be identified with $\mathrm{K}\,.$ in [10]; the second-order time derivative, however, requires additional care in the analysis though.) Clearly, m counts the order of scattering; here, we consider $M = 3$. In a surface seismic experiment, ignoring free-surface effects, we can set $f_- = 0$ (at $z = 0$), while one observes the upcoming wave constituent, $Q_-^*(0)\, \delta u_-(0, ., ., .)$; we model data, d, upon subjecting this constituent further to a restriction to the acquisition geometry.

To develop a framework for inverse scattering, we rewrite (2.12) according to [17, (49)-(50)] as

$$\partial_t^2 \mathsf{G} \widehat{V}\, (U + \delta U) = \delta U.$$

The reconstruction of the contrast is initiated by expanding $\widehat{V}$ into the sum $\widehat{V} = \sum_{m=1}^{M} \widehat{V}_m$. In the actual process, the equation above, and the recursion below, need to be subjected to a restriction to $z = 0$ after applying $Q_-^*(z)$. The reconstruction is usually driven by the single scattering operator derived from δU_1 in (2.13) using all the data; that is,

$$\delta U = \partial_t^2 \mathsf{G}(\widehat{V}_1 U), \tag{2.14}$$

$$-\partial_t^4 \mathsf{G}(\widehat{V}_1 \mathsf{G}(\widehat{V}_1 U)) = \partial_t^2 \mathsf{G}(\widehat{V}_2 U), \tag{2.15}$$

$$-\partial_t^6 \mathsf{G}(\widehat{V}_1 \mathsf{G}(\widehat{V}_1 \mathsf{G}(\widehat{V}_1 U))) - \partial_t^4 \mathsf{G}(\widehat{V}_1 \mathsf{G}(\widehat{V}_2 U)) - \partial_t^4 \mathsf{G}(\widehat{V}_2 \mathsf{G}(\widehat{V}_1 U)) = \partial_t^2 \mathsf{G}(\widehat{V}_3 U),\ \cdots \tag{2.16}$$

In this procedure, $\widehat{V}_2$, $\widehat{V}_3$, .. contain artifacts that correct the initial reconstruction, $\widehat{V}_1$. Here, we assume full illumination through the single scattering operator appearing on the right-hand sides of equations (2.14)-(2.16). If the data acquisition only results in partial illumination, we can complement this illumination by higher-order terms appearing on the left-hand sides of (2.15)-(2.16). For example, the illumination of $\widehat{V}_2$ is the same as of $\widehat{V}_1$; locally, where $\widehat{V}_1$ has not been illuminated through (2.14), one can fill in "holes" by moving the corresponding contribution from the left-hand side in equation (2.15) to the right-hand side of equation (2.14). Indeed, the left-most terms in (2.15)-(2.16) can generate contributions that are effectively of first (or second) order, the next two terms on the left-hand side of (2.16) can generate contributions that are effectively of second order, etc. This approach is elaborated in the following subsection.

2.3. Illumination decomposition. In many configurations, there are regions where $\widehat{V}$ cannot reached by singly scattered waves. Multiple scattered waves may form a remedy for illumination. To analyze this, we introduce the illumination decomposition,

$$\widehat{V}_1 = \widehat{V}_1' + \widehat{V}_1'' + \widehat{V}_1''' + \ldots, \tag{2.17}$$

where $\widehat{V}_1'$ is the part of the model that has been illuminated by the recorded singly scattered data, $\widehat{V}_1''$ is the part of the model that is first illuminated by the doubly scattered data, $\widehat{V}_1'''$ is the part of the model first illuminated by triply scattered data, and so on. In the further analysis, we assume that the wavefront sets of $\widehat{V}_1', \widehat{V}_1'', \widehat{V}_1''', \ldots$ have no points in common. We proceed with a construction to image regions where singly scattered waves do not illuminate the structure of interest; such a construction was carried out for surface-related multiples in [2].

Substituting (2.17) into the expansion for $\widehat{V}$ yields

$$\widehat{V} = \widehat{V}_1' + \widehat{V}_1'' + \widehat{V}_1''' + \cdots + \sum_{m=2}^{M} \widehat{V}_m. \tag{2.18}$$

We note that the illumination decomposition pertains to the higher order terms, $\widehat{V}_2, \widehat{V}_3, \ldots$, associated with the artifacts, as well. Indeed, the artifact prediction is complicated by this decomposition.

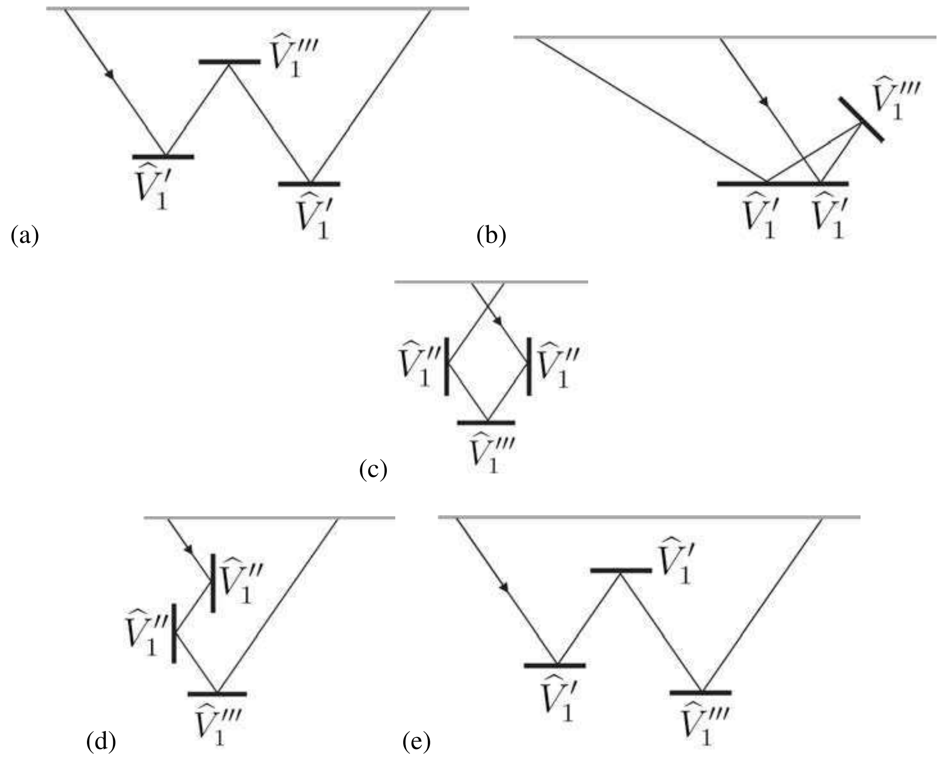

FIG. 2. *Example contributions corresponding with triple scattered illumination; (a) and (b) are admitted, while (c), (d) and (e) are omitted in the construction here, cf. (2.19).*

We adapt the recursion in (2.14)-(2.16), by accounting for illuminating the contrast with multiple scattered waves. With the aid of (2.18), equation (2.14) becomes

$$
\begin{aligned}
(2.19)\quad \delta U = {}& \partial_t^2 \mathsf{G}(\widehat{V}_1' U) + \partial_t^4 \left[\mathsf{G}(\widehat{V}_1' \mathsf{G}(\widehat{V}_1'' U)) + \mathsf{G}(\widehat{V}_1'' \mathsf{G}(\widehat{V}_1' U)) \right] \\
& + \partial_t^6 \Big[\mathsf{G}(\widehat{V}_1' \mathsf{G}(\widehat{V}_1''' \mathsf{G}(\widehat{V}_1' U))) + \mathsf{G}(\widehat{V}_1' \mathsf{G}(\widehat{V}_1' \mathsf{G}(\widehat{V}_1''' U))) + \mathsf{G}(\widehat{V}_1''' \mathsf{G}(\widehat{V}_1' \mathsf{G}(\widehat{V}_1' U))) \\
& + \mathsf{G}(\widehat{V}_1'' \mathsf{G}(\widehat{V}_1''' \mathsf{G}(\widehat{V}_1' U))) + \mathsf{G}(\widehat{V}_1' \mathsf{G}(\widehat{V}_1'' \mathsf{G}(\widehat{V}_1''' U))) + \mathsf{G}(\widehat{V}_1''' \mathsf{G}(\widehat{V}_1' \mathsf{G}(\widehat{V}_1'' U))) \\
& + \mathsf{G}(\widehat{V}_1' \mathsf{G}(\widehat{V}_1''' \mathsf{G}(\widehat{V}_1'' U))) + \mathsf{G}(\widehat{V}_1'' \mathsf{G}(\widehat{V}_1' \mathsf{G}(\widehat{V}_1''' U))) + \mathsf{G}(\widehat{V}_1''' \mathsf{G}(\widehat{V}_1'' \mathsf{G}(\widehat{V}_1' U))) \\
& + \mathsf{G}(\widehat{V}_1'' \mathsf{G}(\widehat{V}_1''' \mathsf{G}(\widehat{V}_1'' U))) + \mathsf{G}(\widehat{V}_1'' \mathsf{G}(\widehat{V}_1'' \mathsf{G}(\widehat{V}_1''' U))) + \mathsf{G}(\widehat{V}_1''' \mathsf{G}(\widehat{V}_1'' \mathsf{G}(\widehat{V}_1'' U))) \Big] + \dots
\end{aligned}
$$

which is then subjected to the restriction to the acquisition geometry in the plane $z = 0$. Naturally, equations (2.15)-(2.16) are affected by this refinement, and more intricate artifact contributions occur.

Down-up reduction. We simplify (2.19) following a seismic experiment. Considering typical scattering ray geometries in combination with a realistic acquisition geometry, we omit contributions that arise in the reconstruction of $\widehat{V}_1'''$ using $\widehat{V}_1''$ (see Figure 2 (c), (d)) – these are less likely to appear in the data. Contributions described by Figure 2 (e) are likely to violate our assumptions concerning $\widehat{V}_1'$ and $\widehat{V}_1'''$. Out of the remaining contributions involving $\widehat{V}_1'''$, the first term is most likely to play a role in practice (see Figure 2 (a) and (b)). We write

$$
(2.20)\qquad \widehat{V} = \begin{pmatrix} \widehat{V}_{++} & \widehat{V}_{+-} \\ \widehat{V}_{-+} & \widehat{V}_{--} \end{pmatrix}.
$$

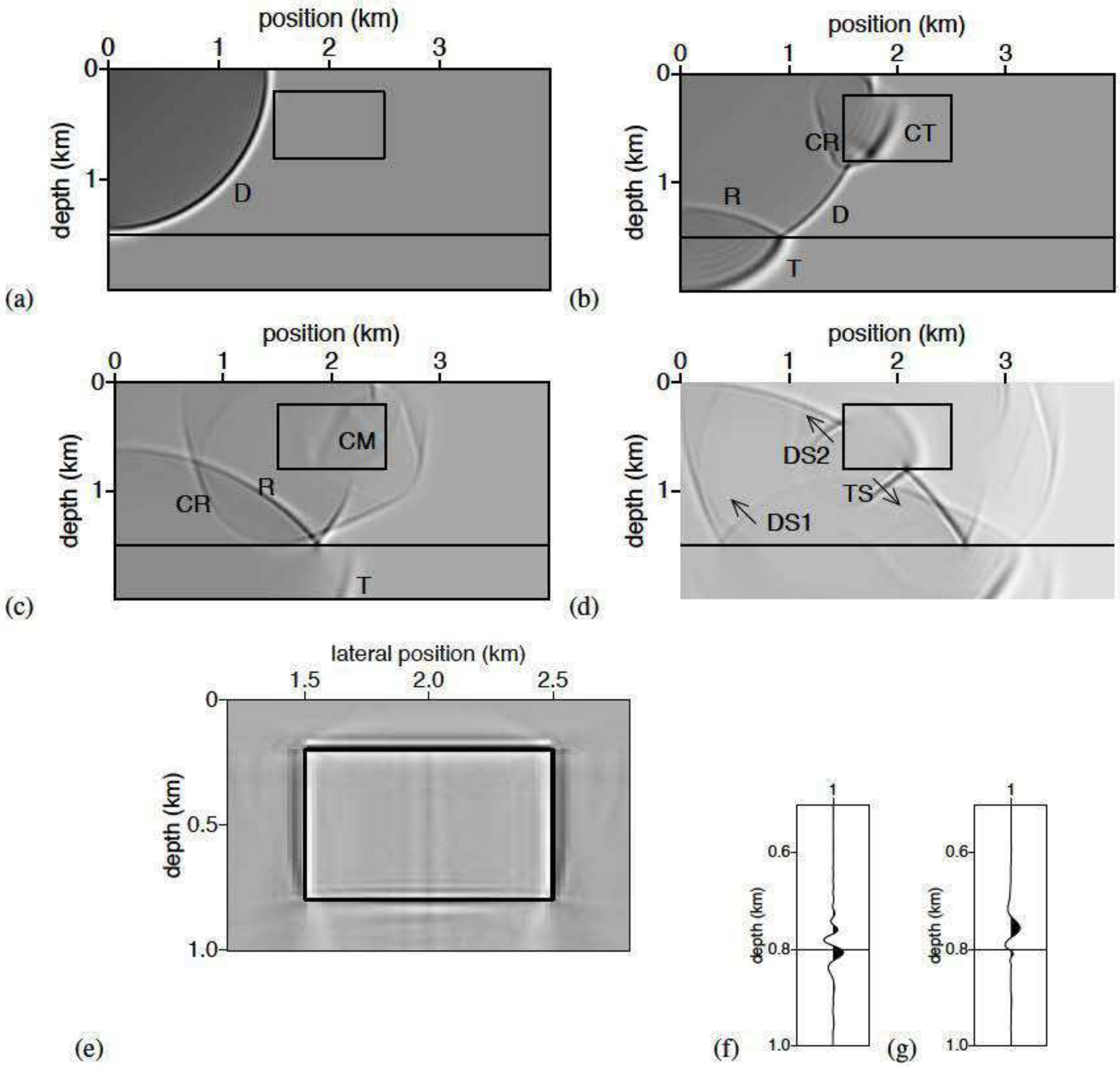

FIG. 3. *Using multiply scattered energy allows the full illumination of an object of interest from surface data. Here we illustrate both the data that are used in the imaging and the resultant images. In (a) through (d) we show snapshots of the wavefield, with time increasing from (a) to (d), as the data are generated. The annotations on the plots highlight different phases used in imaging; 'D' is the direct (downgoing) wave, 'R' is reflected (upcoming) from the lower reflector and 'T' is transmitted through it, 'CR' is the constituent reflected from the cube and 'CT' is the constituent transmitted into it, 'DS1' and 'DS2' are the doubly scattered waves off the left vertical edge of the cube and 'TS' is the underside reflection. In all plots the solid lines mark the positions of reflectors. In (e) we show an image, made assuming constant background velocity, of the cube structure; the vertical edges are imaged with doubly scattered waves ('DS1' and 'DS2' in (d)) and the bottom with triply scattered waves ('TS' in (d)). In (f) and (g) we show that imaging with triply scattered waves – and a constant background velocity – locates the reflector at the correct depth (in (f)), whilst imaging from above, shown in (g), naturally places the reflector at the wrong depth. The traces in (f) and (g) are stacks of images at the base of the cube; the solid line marks the correct reflector location.*

Upon evaluating δU at $z = 0$ and applying $Q_-^*(0)$ to the result, we obtain the data equation

$$(2.21)\quad d = \mathsf{R}\, Q_-^* \partial_t^2 G_- \Big[(\widehat{V}_1')_{-+} + \partial_t^2 (\widehat{V}_1')_{-+}\, G_+\, (\widehat{V}_1'')_{++} + \partial_t^2 (\widehat{V}_1'')_{--}\, G_-\, (\widehat{V}_1')_{-+} + \partial_t^4 (\widehat{V}_1')_{-+}\, G_+\, (\widehat{V}_1''')_{+-}\, G_-\, (\widehat{V}_1')_{-+} \Big] G_+ f_+,$$

where R stands for the restriction to $z = 0$ and d represents the reflection data. We have suppressed the further restriction to the acquisition geometry in our notation. The acquisition geometry consists of a set of sources, s, each with an associated set, Σ_s, of receivers. The terms in this equation can be identified in Figure 3. The second and third terms on the right-hand side are reciprocal to one another. We will make use of equation (2.21) in imaging by a bootstrapping argument. We note that the second and third terms on the right-hand side account for "prismatic" reflections. The focus of this paper is image assimilation based on the first and fourth terms on the right-hand side, thus making use of "underside" reflections. However, we will also briefly address the second and third terms in the discussion.

3. Imaging with multiply scattered waves.

3.1. Projections. We start with the data equation (2.21). Our imaging strategy is as follows. We "project" d onto d_1 in the range of the single scattering operator,

$$d_1 = \mathsf{R}\, Q_-^* \partial_t^2 G_-((\widehat{V}_1')_{-+}(G_+ f_+)), \tag{3.1}$$

by minimizing $\|d - d_1\|$. In the process we reconstruct $(\widehat{V}_1')_{-+}$. We then select a part, $(\dot{\widehat{V}}_1)_{-+}$, of the reconstruction of $(\widehat{V}_1')_{-+}$ to become a scatterer in the background model; this scatterer can be regularized and enhanced with the aid of a curvelet-like transform and methods of ℓ^1 optimization. Using $(\dot{\widehat{V}}_1)_{-+}$, we form a "double" scattering operator by replacing G_- on the right-hand side of (3.1) by

$$\widetilde{G}_{-+}\, . = \partial_t^2 G_-((\dot{\widehat{V}}_1)_{-+}(G_+\, .)). \tag{3.2}$$

We proceed with "projecting" $d - d_1$ onto d_2 in the range of the "double" scattering operator,

$$d_2 = \mathsf{R}\, Q_-^* \partial_t^2 \widetilde{G}_{-+}((\widehat{V}_1'')_{++}(G_+ f_+)), \tag{3.3}$$

by minimizing $\|(d - d_1) - d_2\|$. We reconstruct $(\widehat{V}_1'')_{++}$, and then repeat this step with the reciprocal form,

$$d_2 = \mathsf{R}\, Q_-^* \partial_t^2 G_-((\widehat{V}_1'')_{--}(\widetilde{G}_{-+} f_+)), \tag{3.4}$$

and reconstruct $(\widehat{V}_1'')_{--}$. However, in the vertical acoustic power flux normalization, $\widehat{V}_{--} = \widehat{V}_{++}$, whence we take half the sum of the two double scattering reconstructions. Using $(\dot{\widehat{V}}_1)_{-+}$, we form a "triple" operator by replacing both G_- and G_+ on the right-hand side of (3.1) by $\widetilde{G}_{-+}$. We proceed with "projecting" $d - d_1 - d_2$ onto d_3 in the range of the "triple" scattering scattering operator,

$$d_3 = \mathsf{R}\, Q_-^* \partial_t^2 \widetilde{G}_{-+}((\widehat{V}_1''')_{+-}(\widetilde{G}_{-+} f_+)), \tag{3.5}$$

by minimizing $\|(d - d_1 - d_2) - d_3\|$. We obtain a reconstruction of $(\widehat{V}_1''')_{+-}$.

A natural concern is the separation of the ranges of the different scattering operators. Indeed, an estimate of $(\widehat{V}_1')_{-+}$ made by approximating d with d_1 will differ from the true $\widehat{V}$, by not only the illumination footprint of the acquisition geometry but also by artifacts from higher-order scattering (internal multiples). An approach to attenuate these artifacts is discussed in [17], which can be refined to account for the illumination decomposition introduced here. Moreover, the subtraction of data sets, $d - d_1$, $(d - d_1) - d_2$, and so on, with equations (3.1-3.5) is problematic as the resolution of d_1, d_2, .. will differ from one another.

The approach developed in this paper assumes that singly scattered waves illuminate structures only from above. Where strong vertical gradients exist, however, this assumption can be violated as waves will turn allowing the illumination of near-vertical reflectors (this is exploited in [22, 30, 31]) and, in extreme cases, even illuminating reflectors from below. In principle, we can accommodate these situations by introducing curvilinear coordinates.

3.2. Imaging condition. We revisit the imaging condition from a reverse-time migration perspective, allowing Green's functions in general background models. For each source, the incident field can be written in the form

$$u_s(z, \bar{x}, \omega) = G_+(z, \bar{x}, \omega, 0, s) \tag{3.6}$$

assuming that $f_+(x,\omega) = -\delta(x-s)$. The backpropagated data are given by

$$u_{\Sigma_s}(z,x,\omega) = \int_{\Sigma_s} \overline{G_-(0,r,\omega,z,x)}\, Q_{-,r}(0) d(r,\omega,s)\,\mathrm{d}r; \tag{3.7}$$

the subscript $_r$ in $Q_{-,r}$ signifies that the operator acts in the r, and not the s, variables. We note that the matrix elements of operator $\widehat{V} = \widehat{V}(z) = \widehat{V}(z,x,D_x,D_t)$, such as

$$\widehat{V}_{-+}(z)\,.\; = \mathcal{H}\,Q_-(z)\,(-c_0^{-3}\delta c(z,.)\,(Q_+^*(z)\;.\,)), \tag{3.8}$$

containing the contrast $-c_0^{-3}\delta c$, can be written in terms of their kernels, $\widehat{V}(z,x,\bar{x},\omega)$. We will denote the image of $\widehat{V}_{-+}(z,x,\bar{x},\omega)$ by $\mathcal{I}(z,\bar{x},x,\omega)$. The imaging operator follows from the mapping $d(r,t,s) \mapsto I(z,\bar{x},x)$, where $I(z,\bar{x},x)$ is given by

$$\begin{aligned} I(z,\bar{x},x) = \frac{1}{2\pi}\int \mathcal{I}(z,\bar{x},x,\omega)\,\mathrm{d}\omega &= \frac{1}{2\pi}\int\int \overline{u_s(z,\bar{x},\omega)}\, u_{\Sigma_s}(z,x,\omega)\,\mathrm{d}s\,\omega^2\mathrm{d}\omega \\ &\overset{\omega\to-\omega}{=} \frac{1}{2\pi}\int\int u_s(z,\bar{x},\omega)\,\overline{u_{\Sigma_s}(z,x,\omega)}\,\mathrm{d}s\,\omega^2\mathrm{d}\omega. \end{aligned} \tag{3.9}$$

The second representation is obtained by time reversal. Using that $Q_{+,\bar{x}}(z)^* G_+(z,\bar{x},\omega,0,s)$ can be identified with $G_-(0,s,\omega,z,\bar{x})Q_{-,\bar{x}}(z)$, that is, reciprocity, the first representation attains the form used to image in the downward-continuation approach. With the modelling equation (cf. (3.1))

$$d(r,\omega,s) = Q_{-,r}(0)^*\omega^2 \int\int\int G_-(0,r,\omega,z,x)\widehat{V}_{-+}(z,x,\bar{x},\omega)\,G_+(z,\bar{x},\omega,0,s)\,\mathrm{d}\bar{x}\mathrm{d}x\,\mathrm{d}z, \tag{3.10}$$

we can then form the normal equations and solve the inverse scattering problem by methods of least squares.

A standard calculation shows that an image of $-c_0^{-3}\delta c$ is obtained by setting, in (3.9), $\bar{x} = x$ after replacing $u_s(z,\bar{x},\omega)$ by $Q_{+,\bar{x}}(z)^* u_s(z,\bar{x},\omega)$ and replacing $u_{\Sigma_s}(z,x,\omega)$ by $-\mathcal{H}Q_{-,x}(z)^* u_{\Sigma_s}(z,x,\omega)$. We obtain a form resembling a two-way wave imaging procedure, but u_s does not propagate any $-$ constituents while u_{Σ_s} does not propagate any $+$ constituents. If one were to use a two-way wave propagation procedure, one would filter out the respective constituents by methods of directional decomposition prior to applying the imaging condition to be consistent with the imaging procedure outlined above [11, 29].

One typically modifies the imaging operator derived from $I(z,x,x)$, in accordance with the *common-source* based normalization with the incoming wave amplitude [9],

$$I(z,x) := \int I_s(z,x)\,\mathrm{d}s, \quad I_s^{(1)}(z,x) = \frac{1}{2\pi}\int \frac{1}{|u_s(z,x,\omega)|^2}\overline{u_s(z,x,\omega)}\,u_{\Sigma_s}(z,x,\omega)\,\mathrm{d}\omega. \tag{3.11}$$

This modification can be refined in accordance with a common-source (asymptotic) true-amplitude imaging condition:

$$\begin{aligned} I_s^{(2)}(z,x) = \frac{1}{2\pi}\int &\frac{1}{|u_s(z,x,\omega)|^2} \\ &\sum_{j=0}^{n} \overline{(A_j(z,x,\partial_x,\omega)u_s)(z,x,\omega)}\,(A_j(z,x,\partial_x,\omega)u_{\Sigma_s})(z,x,\omega)\,(-\mathrm{i}\omega)^{-1}S(\omega)\mathrm{d}\omega, \end{aligned} \tag{3.12}$$

where $A_0(z,x,\partial_x,\omega) = \mathrm{i}\omega c_0(z,x)^{-1}$, $A_1(z,x,\partial_z,\partial_x,\omega) = \partial_z$, and $A_{j+1}(z,x,\partial_z,\partial_x,\omega) = \partial_{x_j}$, $j = 1,\ldots,n-1$; $S(\omega) = \omega^{-2}$ if $n = 2$. This imaging condition also annihilates wave constituents that propagate from the source at $(0,s)$ towards (z,x), which follows upon substituting asymptotic ray representations for the Green's functions.

Following the common-source least-squares formulation, leads to the modification

$$I_s^{(3)}(z,x) = \left[\int |u_s(z,x,\omega)|^2\omega^4\mathrm{d}\omega\right]^{-1}\frac{1}{2\pi}\int \overline{u_s(z,x,\omega)}\,u_{\Sigma_s}(z,x,\omega)\,\omega^2\mathrm{d}\omega; \tag{3.13}$$

essentially the gradient (image) is scaled with (an estimate of) the diagonal of the Hessian [21]; see also [23]. This approach can be extended to a least-squares formulation for *all sources and receivers combined*.

So far, we have consider the imaging and (least-squares) reconstruction of $(\widehat{V}_1')_{-+}$ according to (3.1). We can immediately generalize the procedure to the other reconstructions. For example, to reconstruct $(\widehat{V}_1''')_{+-}$, one replaces G_- and G_+ both by $\widetilde{G}_{-+}$. We note that the computation of the latter operator makes use of the prior reconstruction of $(\widehat{V}_1')_{-+}$.

3.3. Algorithm summary. The proposed algorithm can be summarized as follows:

1. we downward/forward propagate the "source" wavefield, u_s, and downward/backward propagate the "receivers" wavefield, u_{Σ_s};
2. we store both u_s and u_{Σ_s} at each depth;
3. we apply imaging condition (3.13) to obtain an estimate for $-c_0^{-3}\delta c$ throughout the model;
4. with the estimate of $-c_0^{-3}\delta c$ we form operators $\widehat{V}_{-+}$, cf. (3.8), and apply these to u_s and u_{Σ_s} at each depth;
5. we, accumulatively, propagate the outcomes of the previous step upward to form $\widetilde{u}_s$ (forward) and $\widetilde{u}_{\Sigma_s}$ (backward); $\widetilde{u}_s$ is obtained from u_s upon replacing G_+ by $\widetilde{G}_{-+}$, and $\widetilde{u}_{\Sigma_s}$ is obtained from u_{Σ_s} upon replacing $\overline{G_-}$ by $\overline{\widetilde{G}_{-+}}$;
6. we apply the imaging condition, using $\widetilde{u}_{\Sigma_s}$ and u_s to estimate $-c_0^{-3}\delta c$ in accordance with (3.3), and using $\widetilde{u}_{\Sigma_s}$ and $\widetilde{u}_s$ to estimate $-c_0^{-3}\delta c$ in accordance with (3.5).

All computations are carried out in the frequency domain. In the above, we have omitted the subtraction, $d - d_1$ for the imaging with doubly scattered waves, and $d - d_1 - d_2$ for the imaging with triply scattered waves. This is motivated by computational efficiency. The idea is to apply pseudodifferential cutoffs to the downward continued fields, chosen in accordance with the reliable part of the background velocity model, prior to applying the imaging condition to mimic the subtraction. One such a cutoff is illustrated in Figure 4 in the case of double scattering. The representative model consists of a vertical reflecting segment, and a deep, extended horizontal reflector. In (b) the backpropagated field u_{Σ_s} is shown at a certain depth (300 m, here); clearly d_1 (reflection off the bottom reflector) and d_2 ("prismatic" reflection) components are present. By applying a left-right separating "dip" filter (in (c)), the two components separate sufficiently to prevent constructive correlation with $\widetilde{u}_s$, which is illustrated in (e) and is subjected to left-right separating "dip" filtering as well (in (f)). For comparison, we show the outcome of the subtraction procedure proper in (i). We note that the images obtained with filtering (in (h)) and with subtraction (in (i)) are very close to one another. The effect of ignoring the subtraction alltogether is illustrated in the image in (g).

The cutoff used to mimic the subtraction $d - d_1 - d_2$ in the case of a typical triple scattering situation is illustrated in Figures 5-6. The representative model consists of a shallow horizontal reflecting segment, and a deep, extended horizontal reflector. Small offsets can be used to generate, locally, $\dot{\widehat{V}}_1$, while large offsets are used in the imaging with underside reflections that have not passed through the region right above the horizontal segment.

To replace the subtraction with d_1, a straightforward windowing procedure is applied as illustrated in Figure 5. The windowing is carried out while the data are downward continued, by removing a window of time before times where energy from multiples is expected. Figures 5 (b)-(e) show the data (u_{Σ_s}) at the depth of the upper reflector (segment); it is here that applying the imaging condition should result in the imaging (from below) of this reflector. In Figure 5 (b) the data are shown without the windowing procedure, so that the primary from the lower reflector is still visible, resulting in an artifact in the associated image (in Figure 6 (a)). In Figure 5 (c) the results of applying the windowing procedure are shown; despite the simplicity of this procedure, we note that the artifacts are attenuated in image shown in Figure 6 (b) (for short offsets only; in Figure 6 (b') for long offsets only). For comparison, in Figure 6 (c), we show the image obtained with the subtraction procedure. In Figure 5 (e) we illustrate $\widetilde{u}_s$ at the depth of the upper reflector – no windowing needs to be applied.

For the examples shown in the next section, the window (cutoff) was slightly modified in as much as that the length of the time window was a linear function of the source-receiver offset.

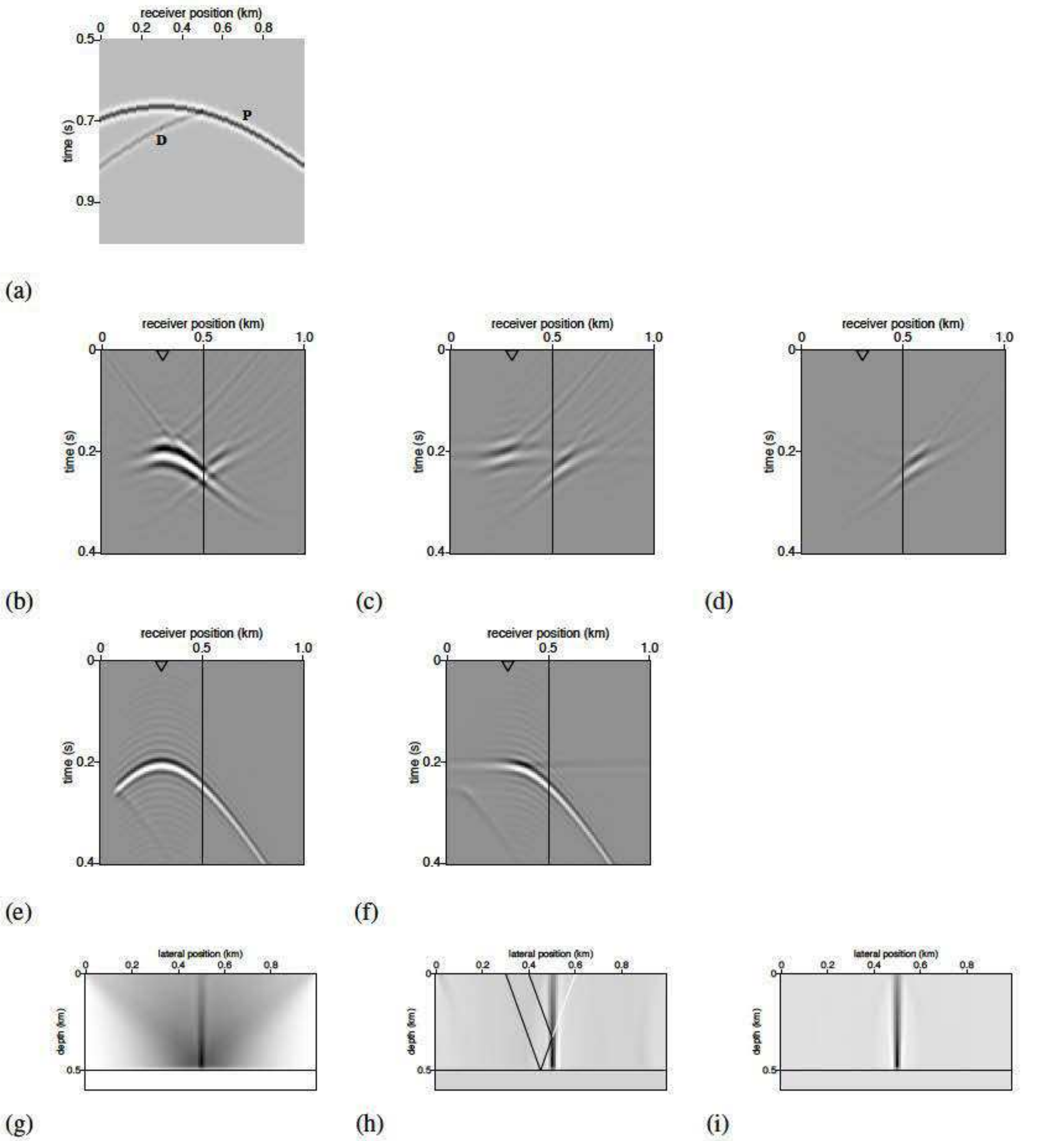

FIG. 4. *(a) Shot record, with source* s *at 300 m (indicated by a trangle in (b)-(f)); 'P' marks the primary reflection off the bottom reflector and 'D' marks the doubly scattered wave; (b) the field u_{Σ_s} at a depth of 300 m (the vertical line indicates the fault offset); (c) the field u_{Σ_s} at a depth of 300 m subjected to left-right "dip" filtering, suppressing the white ray in (g); (d) the field u_{Σ_s} at a depth of 300 m generated from $d - d_1$; (e) the field $\widetilde{u}_s$ at a depth of 300 m; (f) the field $\widetilde{u}_s$ at a depth of 300 m subjected to left-right "dip" filtering; (g) image generated omitting the subtraction procedure; (h) image generated with the filtering; (i) image generated with the subtraction procedure.*

4. Numerical experiments: Imaging with underside reflections. In this and the next sections, we present several synthetic data examples to demonstrate the utility of the method discussed above. The data were generated using a 2D finite difference code; they were then filtered with a trapezoidal filter with corner frequencies 10 and 50 Hz and 10 Hz roll-off. The sources and receivers are positioned on (different) fixed grids. Table 4.1 summarizes the parameters used for each of the subsequent models used in the numerical experiments.

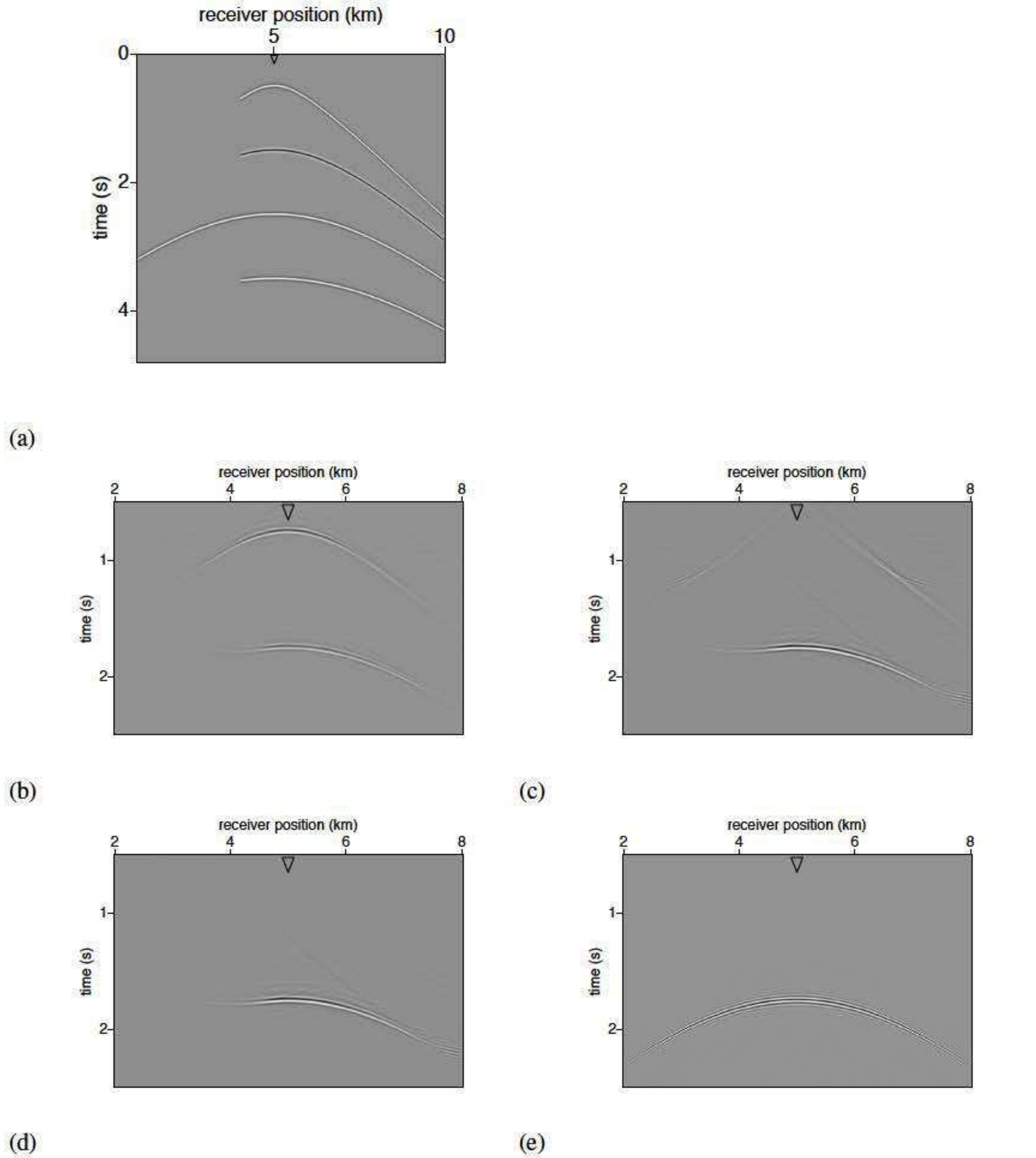

FIG. 5. *(a) Shot record, with source s at 5000 m (indicated by a trangle in (b)-(e)); (b) the field u_{Σ_s} at a depth of 1500 m; (c) the field u_{Σ_s} at a depth of 1500 m subjected to time-windowing, suppressing the white ray in (g); (d) the field u_{Σ_s} at a depth of 1500 m generated from $d - d_1(-d_2)$; (e) the field $\widetilde{u}_s$ at a depth of 1500 m.*

model	first r (km)	Δr (m)	# receivers	first s (km)	Δs (m)	# sources
salt without inclusions	0	20	650	2.0	100	80
salt with inclusions	0	20	650	1.0	100	110
fault	0	20	550	0	100	110

TABLE 4.1
Parameters used to generate the example synthetic data sets.

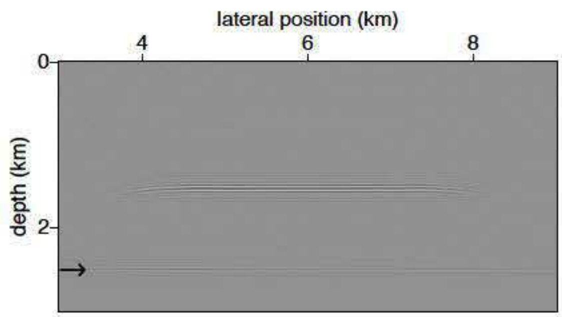

(a)

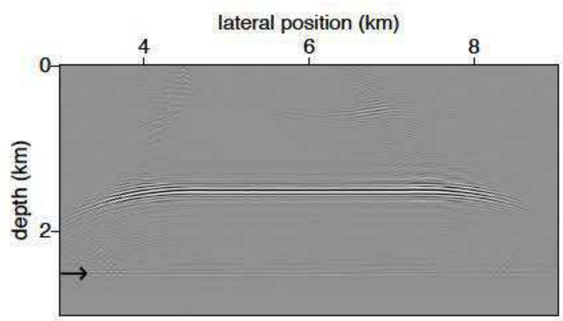

(b)

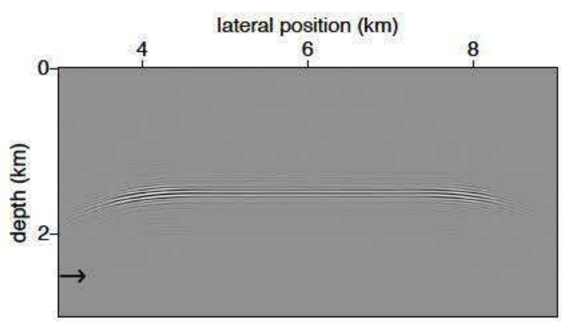

(c)

FIG. 6. *(a) Image generated omitting the subtraction procedure; (b) image generated with the windowing; (c) image generated with the subtraction procedure. The arrow indicates the depth of the bottom reflector.*

A problem of current interest in sub-salt imaging is the location of the bottom of salt when the salt itself is non-uniform. Multiples can illuminate these structures without passing through them, however, which has the potential to locate the salt bottom without first determining an accurate salt model. To test this scenario, we developed a salt model in which the salt contains sediment inclusions; we then study the influence of these inclusions on the location of the bottom of salt both with singly and triply scattered waves. We generated data in two models: the 'inclusion model' and the 'inclusion-free model'. The inclusion model is shown in Figure 7 (a); the inclusion-free model differs only in the absence of the inclusions. Figure 8 shows two images, made with data generated in the inclusion model, one using the inclusion model and the

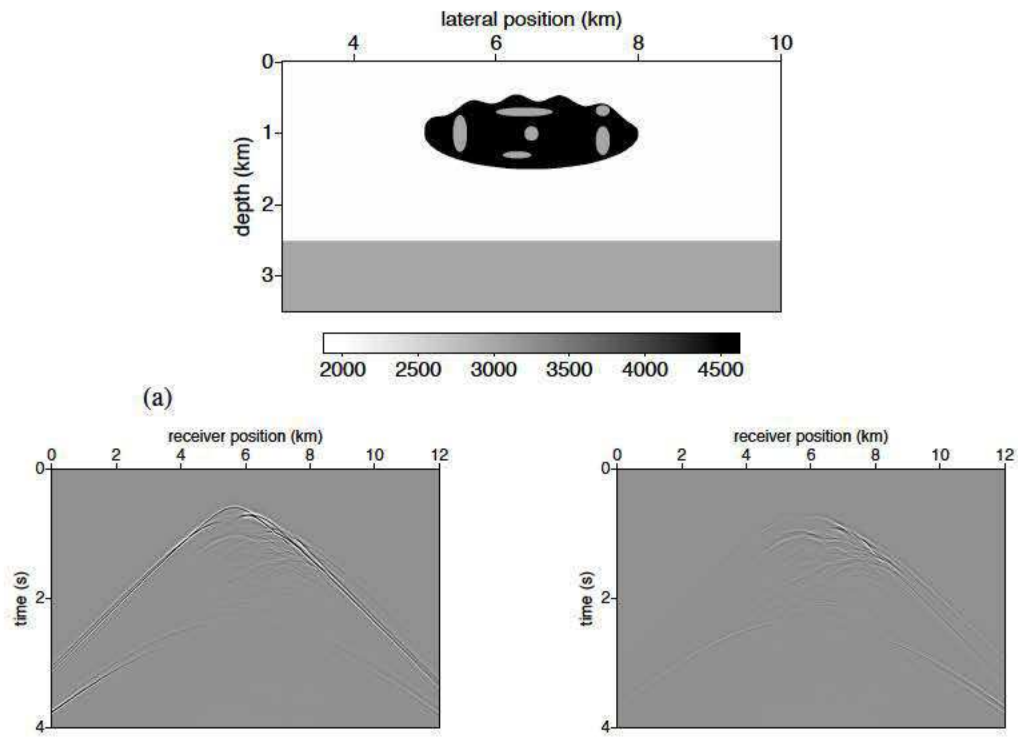

(a)

(b) (c)

FIG. 7. *(a) Velocity model for the salt example; (b) shot record at* $s = 5.5$ *km; (c) difference between shot records with and without inclusions.*

other using the inclusion-free model. If the inclusions are unknown, we observe that the image of the base of salt deteriorates significantly, as expected.

In Figure 9 we illustrate that internal multiples can indeed image the base of salt. The main advantage of imaging with internal multiples is that in some instances they reflect off the base and flanks of the salt without passing through it, allowing imaging without knowing the structure of the salt. To test this, we restrict the source/receiver locations to avoid waves that pass through the salt. This is illustrated in Figure 9 (a)-(c); in Figure 9 (a) the left flank of the salt is imaged using sources (whose range is denoted with the black line) and receivers (whose range is denoted with the white line and extends to 0 off the edge of the plot) to the left of the salt body. This restricts our wave paths to those illustrated in Figure 2 (b). In Figure 9 (b) the sources are to the left of the salt and the receivers to the right, focusing on paths like those illustrated in Figure 2 (a); we observe that the base of salt is well imaged. Figure 9 (c) shows a reconstruction of the lower half of the salt body formed by summing three images made using different source/receiver geometries.

In Figure 10 we demonstrate the insensitivity of our procedure to errors in the velocity model. Figures 10 (a)-(c) are analogous to Figures 9 (a)-(c) with the exception that the data were modeled in the inclusion model. These data were still imaged using the inclusion-free model and yet the (partial) images remain of the same quality as those shown in Figure 9 where there were no inclusions. The images in Figure 10 (c) and Figure 8 (a) compare favorably.

5. Discussion. Multiply scattered waves have the ability to contribute useful information to seismic images. Because they can illuminate structures not easily illuminated by primaries, these waves allow us to image portions of the subsurface not illuminated by singly scattered energy. By including the illumination footprint of the acquisition geometry from the beginning of our, series based, data representation we are able to isolate the contributions from different orders of scattering. Once these contributions are isolated it

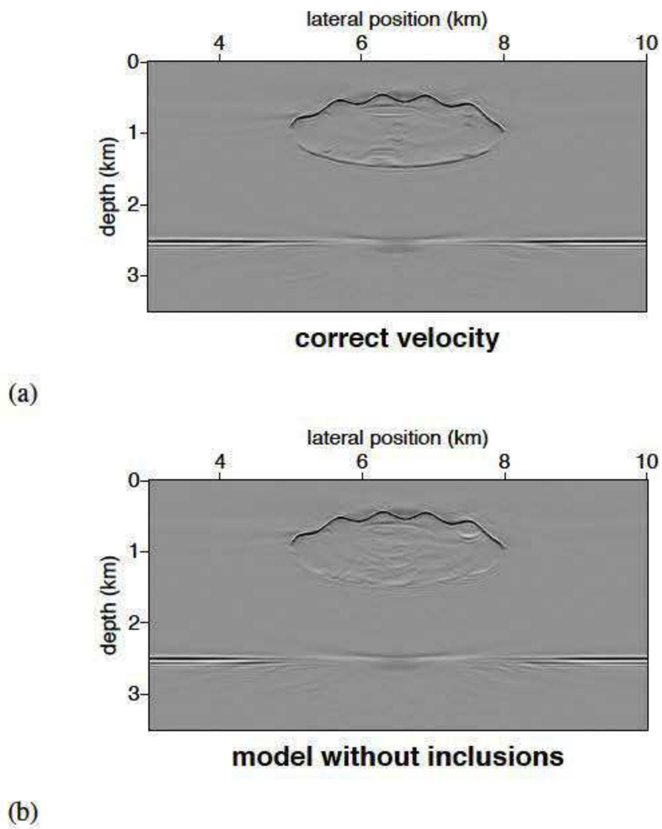

FIG. 8. *(a) Image based on primary reflections made with the correct velocity model using the model and data illustrated in Figure 7 – the best image we can expect to make of the bottom of the salt; (b) image based on primary reflections made with the inclusion-free velocity model.*

is possible to develop an algorithm to treat each order of multiple scattering separately. It is important to note, however, that the resulting algorithms are quite similar and can in fact be combined into one multiple-scattering imaging algorithm. We focussed on the use of "underside" reflections, but "prismatic" reflection are included in our approach as well.

Imaging with "prismatic" reflections. Along with subsalt imaging from below, the appoach presented above also allows the imaging of steeply dipping reflectors with doubly scattered waves in a manner similar to the one discussed by [14]. In a numerical experiment, here, we focus on imaging faults. The model, shown in Figure 11, consists of sedimentary layers with simple topography cut through by a fault structure. A standard image based on primary reflection is also shown in Figure 11, in which the fault's location is perhaps discernible but it has not been imaged. This figure also shows the difference of two images made with doubly scattered waves, one with waves reflected off the left side of the fault and the other with waves reflected off the right side of the fault. This doubly scattered image is then assimilated with the regular image resulting in an image where near-vertical and near-horizontal structures are well resolved.

We have presented a computational and processing-based approach to image with multiply scattered waves. We anticipate the key applications to occur in subsalt imaging, but incorporation of multiply scattered waves in migration velocity analysis seems feasible along the same line of reasoning.

Acknowledgment. MVdH was supported in part by the members of the Geo-Mathematical Imaging Group.

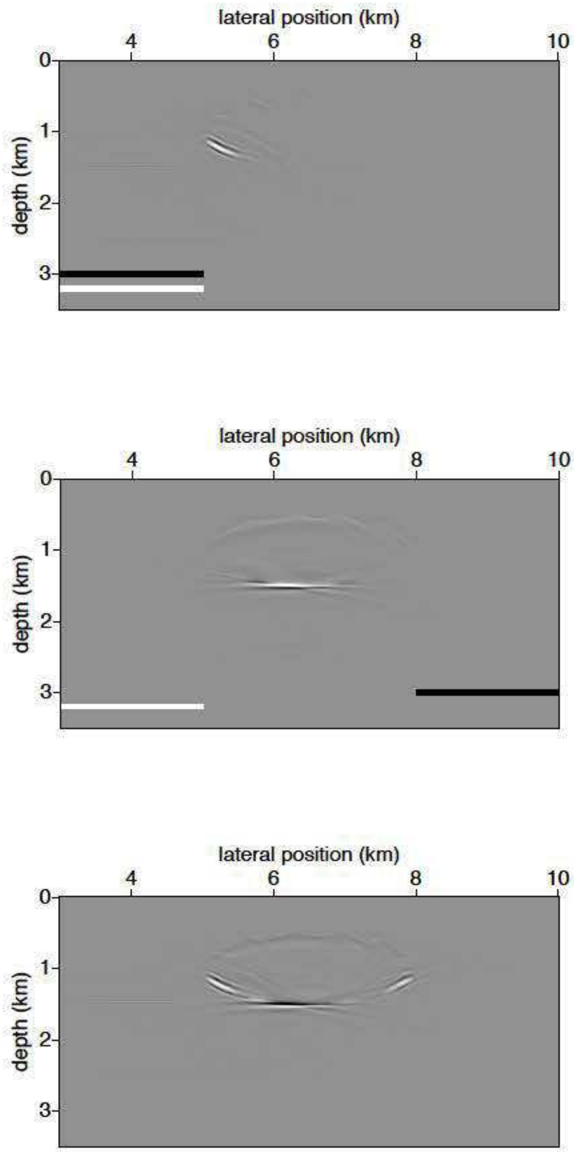

(a)

(b)

(c)

FIG. 9. *Imaging with underside reflections, using data generated in the model without inclusions; (a) left lower flank of the salt imaged using sources (whose range is denoted with the black line) and receivers (whose range is denoted with the white line and extends to 0 off the edge of the plot) to the left of the salt body – wave paths corresponding with Figure 2 (b); (b) bottom of the salt imaged using sources to the left of the salt and receivers to the right, focusing on paths like those illustrated in Figure 2 (a); (c) reconstruction of the lower part of the salt body formed by adding (a), (b) and an image generated like (a) but with sources and receiver to the right of the salt body.*

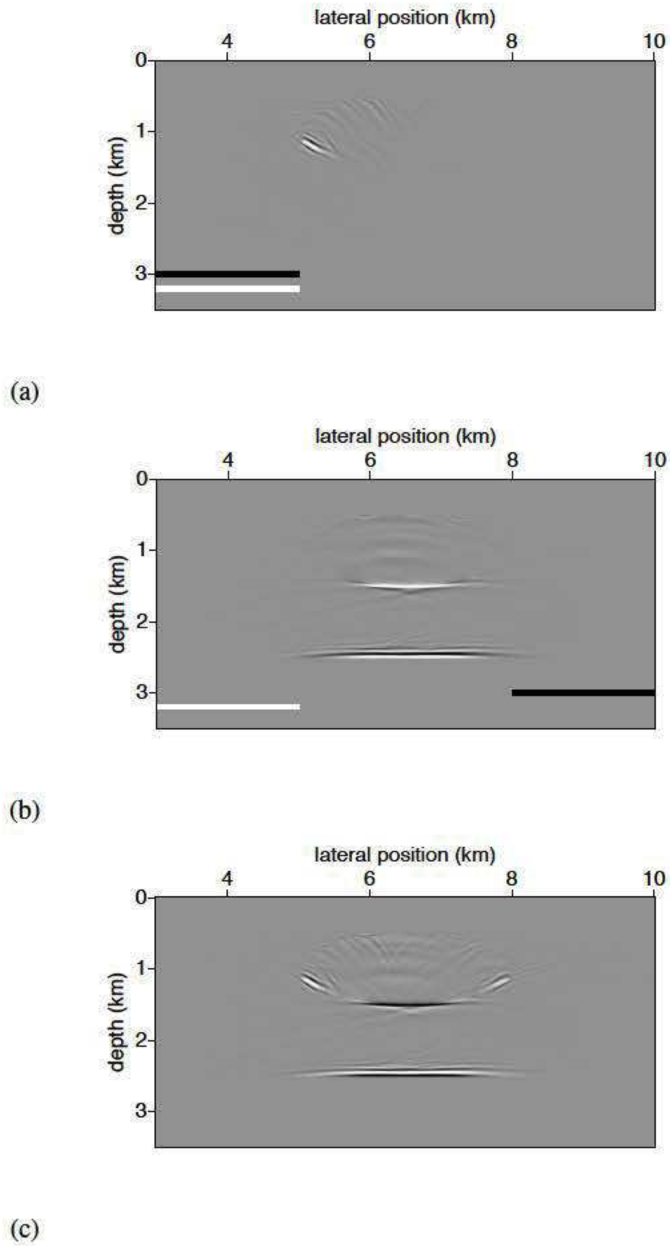

FIG. 10. *Imaging using the inclusion-free model as velocity model with underside reflections, using data generated in the model with inclusions; (a) left lower flank of the salt imaged using sources (whose range is denoted with the black line) and receivers (whose range is denoted with the white line and extends to 0 off the edge of the plot) to the left of the salt body – wave paths corresponding with Figure 2 (b); (b) bottom of the salt imaged using sources to the left of the salt and receivers to the right, focusing on paths like those illustrated in Figure 2 (a); (c) reconstruction of the lower part of the salt body formed by adding (a), (b) and an image generated like (a) but with sources and receiver to the right of the salt body.*

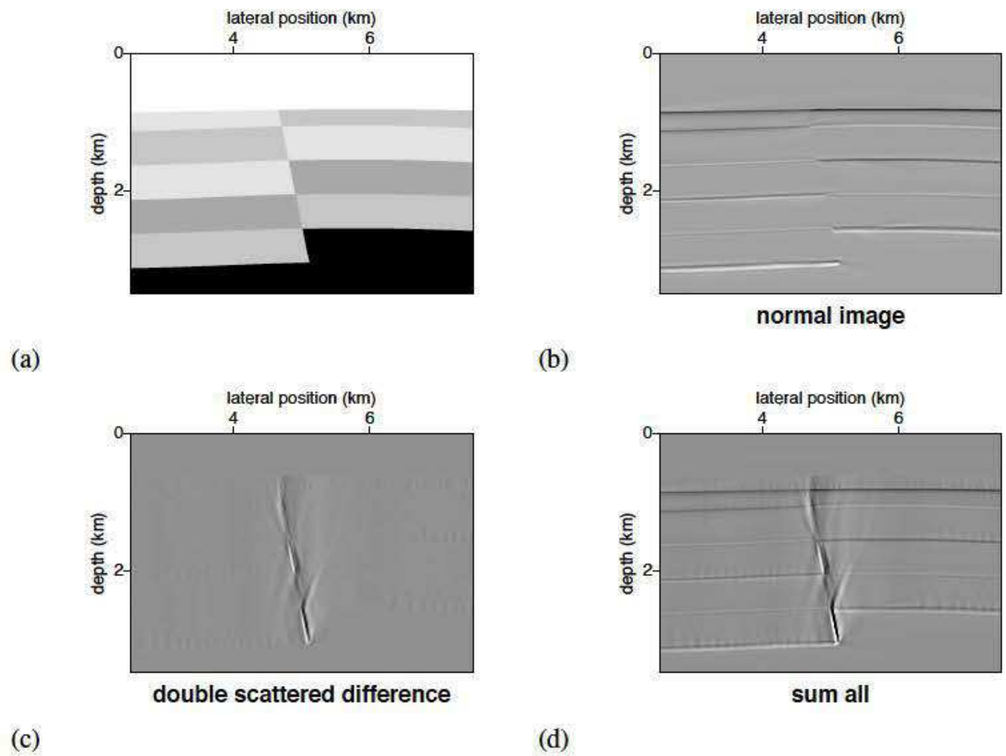

FIG. 11. *(a) Velocity model for the fault model; (b) standard image based on primary reflections; (c) image based on prismatic reflections (doubly scattered waves), taking the difference of the left and right scattered contributions; (d) the sum of (b) and (c).*

REFERENCES

[1] DAVID W. BELL, *Seismic imaging of steeply dipping geologic interfaces*, United States patent, (1991).

[2] A. J. BERKHOUT AND D. J. VERSCHUUR, *Imaging of multiple reflections*, Geophysics, 71 (2006), pp. SI209–SI220.

[3] BIONDO BIONDI AND GUOJIAN SHAN, *Prestack imaging of overturned reflections by reverse time migration*, SEG Technical Program Expanded Abstracts, 21 (2002), pp. 1284–1287.

[4] M. G. BOSTOCK, S. RONDENAY, AND J. SHRAGGE, *Multiparameter two-dimensional inversion of scattered teleseismic body waves 1. theory for oblique incidence*, Journal of Geophysical Research, 106 (2001), pp. 30771–30782.

[5] H. BREMMER, *The W. K. B. approximation as the first term of a geometric-optical series*, Communications on Pure and Applied Mathematics, 4 (1951), pp. 105–115.

[6] KARINE BROTO AND PATRICK LAILLY, *Towards the tomographic inversion of prismatic reflections*, SEG Technical Program Expanded Abstracts, 20 (2001), pp. 726–729.

[7] MAUD CAVALCA AND PATRICK LAILLY, *Prismatic reflections for the delineation of salt bodies*, SEG Technical Program Expanded Abstracts, 24 (2005), pp. 2550–2553.

[8] ———, *Accounting for the definition domain of the forward map in traveltime tomography – application to the inversion of prismatic reflections*, Inverse Problems, 23 (2007), pp. 139–164.

[9] JON F. CLAERBOUT, *Toward a unified theory of reflector mapping*, Geophysics, 36 (1971), pp. 467–481.

[10] M. V. DE HOOP, *Generalization of the Bremmer coupling series*, J. Math. Phys., 37 (1996), pp. 3246–3282.

[11] ROBIN P. FLETCHER, PAUL J. FOWLER, PHIL KITCHENSIDE, AND UWE ALBERTIN, *Suppressing unwanted internal reflections in prestack reverse-time migration*, Geophysics, 71 (2006), pp. E79–E82.

[12] DAVE HALE, N. ROSS HILL, AND JOSEPH P. STEFANI, *Imaging salt with turning seismic waves*, SEG Technical Program Expanded Abstracts, 10 (1991), pp. 1171–1174.

[13] K. HAWKINS, *The challenge presented by North Sea Central Graben salt domes to all DMO algorithms*, First Break, 12 (1994), pp. 327–343.

[14] SHENGWEN JIN, SHIYONG XU, AND DAVID WALRAVEN, *One-return wave equation migration: Imaging of duplex waves*, SEG Technical Program Expanded Abstracts, 25 (2006), pp. 2338–2342.

[15] B. A. LIPPMANN, *Variational principles for scattering processes II scattering of slow neutrons by para-hydrogen*, Phys. Rev., 79 (1950), pp. 481–486.

[16] B. A. LIPPMANN AND J. SCHWINGER, *Variational principles for scattering processes I*, Phys. Rev., 79 (1950), pp. 469–480.

[17] A. E. MALCOLM AND M. V. DE HOOP, *A method for inverse scattering based on the generalized Bremmer coupling series*, Inverse Problems, 21 (2005), pp. 1137–1167.

[18] NAUM MARMALYEVSKYY, YURY ROGANOV, ZINOVY GORNYAK, ALEX KOSTYUKEVYCH, AND VIKTOR MERSHCHIY, *Migration of duplex waves*, SEG Technical Program Expanded Abstracts, 24 (2005), pp. 2025–2028.

[19] R. MITTET, *The behaviour of multiples in reverse time migration*, in Expanded Abstracts, Eur. Assn. Geoscient. Eng., 2006.

[20] C. J. NOLAN, M. CHENEY, T. DOWLING, AND R. GABURRO, *Enhanced angular resolution from multiply scattered waves*, Inverse Problems, 22 (2006), pp. 1817–1834.

[21] R.-E. PLESSIX AND W. MULDER, *Frequency-domain finite-difference amplitude-preserving migration*, Geophysical Journal International, 157 (2004), pp. 975–987.

[22] GUOJIAN SHAN AND BIONDO BIONDI, *Imaging overturned waves by plane-wave migration in tilted coordinates*, SEG Technical Program Expanded Abstracts, 23 (2004), pp. 969–972.

[23] C. SHIN, S. JANG, AND D.-J. MIN, *Improved amplitude preservation for prestack depth migration by inverse scattering theory*, Geophysical Prospecting, 49 (2001), pp. 592–606.

[24] J. SJÖSTRAND AND A. GRIGIS, *Microlocal Analysis for Differential Operators: An Introduction*, Cambridge University Press, Cambridge, 1994.

[25] C. C. STOLK AND M. V. DE HOOP, *Seismic inverse scattering in the downward continuation approach*, Wave Motion, 43 (2006), pp. 579–598.

[26] C. C. STOLK AND M. V. DE HOOP, *Curvilinear wave-equation angle transform: Caustics, turning rays, absence of kinematic artifact*, in Expanded Abstracts, Society of Exploration Geophysicists, 2007, pp. 2180–2183.

[27] A. WEGLEIN, F. B. ARAÚJO, P. M. CARVALHO, R. H. STOLT, K. H. MATSON, R. T. COATES, D. CORRIGAN, D. J. FOSTER, S. A. SHAW, AND H. ZHANG, *Inverse scattering series and seismic exploration*, Inverse Problems, 19 (2003), pp. R27–R83.

[28] A. WEGLEIN, F. A. GASPAROTTO, P. M. CARVALHO, AND R. H. STOLT, *An inverse-scattering series method for attenuating multiples in seismic reflection data*, Geophysics, 62 (1997), pp. 1975–1989.

[29] XIAO-BI XIE AND RU-SHAN WU, *A depth migration method based on the full-wave reverse-time calculation and local one-way propagation*, SEG Technical Program Expanded Abstracts, 25 (2006), pp. 2333–2337.

[30] S. XU AND S. JIN, *Wave equation migration of turning waves*, SEG Technical Program Expanded Abstracts, 25 (2006), p. 2328.

[31] Y. ZHANG, S. XU, AND G. ZHANG, *Imaging complex salt bodies with turning-wave one-way wave equation*, SEG Technical Program Expanded Abstracts, 25 (2006), p. 2323.